Non Invasive Measurement on the Pulsed and Steady-State, High Power MadHeX Helicon Plasma Thruster

IEPC-2009-206

Presented at the 31st International Electric Propulsion Conference,
University of Michigan, Ann Arbor, Michigan, USA
September 20–24, 2009

Matt Wiebold*, John E. Scharer† and He Ren‡
University of Wisconsin - Madison, Madison, WI 53711

Abstract: Non-invasive measurements are performed on a pulsed and steady-state argon helicon plasma thruster with a static axial magnetic nozzle field (1 kG source, 1.5 kG nozzle peak). Flow rates are between 1 and 76 sccm with coupled 13.56 MHz rf power levels of between 700 W and 10 kW. Collisional-radiative (CR) models for Ar II and Ar I are used to spectroscopically determine the electron temperature (Te) and the neutral density, respectively. The electron density (n_{emax}= 8 x 10^{13}/cm^{-3}) is measured via 105 GHz microwave interferometry and is an input to the CR models. In collisionless, highly neutral-depleted regions, T_e rises linearly with power while ne remains constrained. Regions of pressure balance and pressure gradients are present, and evidence of substantial axially accelerated ion flows is observed. Regimes where cooler (5 eV) and hotter (>20 eV) electron temperatures are observed for lower and higher flow rates. The axial ion energy distribution function and its acceleration is measured in these different regimes from the source region through the nozzle using tunable diode laser-induced fluorescence.

Nomenclature

LIF	= laser induced fluorescence
MOPA	= master oscillator power amplifier
rf	= radiofrequency
n_e	= electron density
n_n	= neutral density
p_n	= neutral pressure
p_e	= electron pressure
p_{tot}	= total pressure
p_i	= ion pressure
T_e	= electron temperature
PMT	= photomultiplier tube

*Ph.D. Candidate, Electrical and Computer Engineering Department, wiebold@wisc.edu
†Professor, Electrical and Computer Engineering Department, scharer@engr.wisc.edu
‡Masters Candidate, Electrical and Computer Engineering Department, ren4@wisc.edu

I. Introduction

THE helicon plasma source is high density, high efficiency rf plasma source, which is a highly efficient method (80-90%) for creating high-density, low-temperature, steady-state plasma from gaseous propellants.[1] Helicon plasma sources have been the subject of much theoretical and experimental work because of their ability to efficiently produce high-density plasma. A helicon plasma source generates an order of magnitude higher plasma density than a DC electron bombardment source of equivalent power. Typical plasma densities associated with helicon plasma discharges are 10^{12} - 10^{14} cm^{-3} with ionization fractions approaching unity (>92% line averaged in our case in argon with < 1 kW input power). Helicon sources are thus capable of realizing ionization costs approaching the theoretical minimum, which is almost a factor of ten lower than that obtained in traditional Hall effect thrusters. Plasma production is sustained by propagation and absorption of helicon waves (cylindrically-bounded whistler waves) in magnetized plasma. In order to launch the wave into the plasma, an axial magnetic field (that can be produced by low mass, non-power consuming ceramic magnets) is applied in the ionization region and a rf antenna surrounding the plasma column couples to the plasma. The magnetic field direction and the antenna geometry determine the resultant wave propagation direction and wave pattern.

The basic configuration of a helicon plasma source is a cylindrical chamber with an axial magnetic field in the 20-5000 Gauss range and one of various types of rf antennae operating at a frequency between the ion and electron cyclotron frequencies. The creation of plasma allows the antenna to excite a helicon wave, and the mechanisms that may couple to fast electrons and provide enhanced ionization have[2–4] and are currently being examined by our research group.

The fundamental physical processes that account for extremely efficient helicon operation[5] in different operating regimes have been under investigation and are of considerable current interest. Collisional processes and Landau damping examined by our group,[6] helicon wave penetration,[7] antenna localized acceleration,[8,9] nonlinear trapping of fast electrons,[10,11] a theory of heating via non-linear coupling to ion acoustic modes,[12–14] and ion heating[15] have all been examined for different operating regimes. Previous collaborative research with the Australian National University (ANU) Boswell and Charles group[2] examined excited-state Ar II optical emission and wave magnetic fields that indicate that non-Maxwellian fast electrons (25-52 eV) can play an important role in ionization processes on the WOMBAT helicon experiment. Modeling with complementary ionization codes, antenna and plasma wave field codes support the presence of non-Maxwellian fast electron distributions in certain regimes. Our research then focused on a double half-turn helix antenna helicon experiment at the University of Wisconsin.[3] We examined the changing plasma axial and radial density and temperature profile characteristics and substantial changes in the correlation between the excited Ar II optical emission and the helicon wave that indicate fast electron components in the helicon source distribution. Ahedo has shown that fast electron components will benefit thruster performance.[16] This occurs as the source changes from the "transition mode" to a high-density intense "blue mode" as the static magnetic field and coupled RF power are increased. We have carried out research on neutral depletion and the associated plasma flow in these sources using a new, state-of-the-art, non-invasive spectroscopic diagnostic. This has enabled us to make initial measurements of axial variations of electron temperature, neutral density, plasma and neutral pressure gradients and the associated enhanced plasma flow.[17]

Our research group has also examined the effects of a non-uniform magnetic field in an experiment characterized by a magnetic cusp located on the upstream side of the antenna and, on the downstream side, an increasing magnetic mirror field as one moves away from the antenna.[18] Compared to a uniform field, substantial enhancements were observed in the electron temperature and thermal anisotropy, plasma β and confinement.

II. MadHeX Helicon Thruster Experiment

A. Overview

The MadHeX system has been operated at powers up to 10 kW and produces densities in the 10^{13} cm^{-3} range with average energy electron temperatures up to 20 eV. It also exhibits full ionization in the core (92% line averaged), based on current and earlier measurements of the coupled RF power and plasma density profiles as well as plasma acceleration and axial flow of several km/s at even low RF powers <1 kW.

Figures 1 and 2 depict the experiment. The vacuum chamber consists of a 10-cm-inner-diameter Pyrex

tube (1.5 m long) and tee section (46 cm long) terminated by grounded aluminum plates on both ends, located at z = -91 cm and 105 cm, where z = 0 is the downstream edge of the antenna and the positive-z direction points in the direction of gas flow. An 18-cm-long, half-turn double-helix antenna wrapped around the Pyrex chamber couples in 13.56 MHz RF power at levels up to 10 kW in CW and pulsed operation. We have also constructed a larger diameter (0.5 m) space chamber to provide a pressure differential from the helicon source region and to accommodate the magnetic field line expansion with substantially reduced neutral reflux.

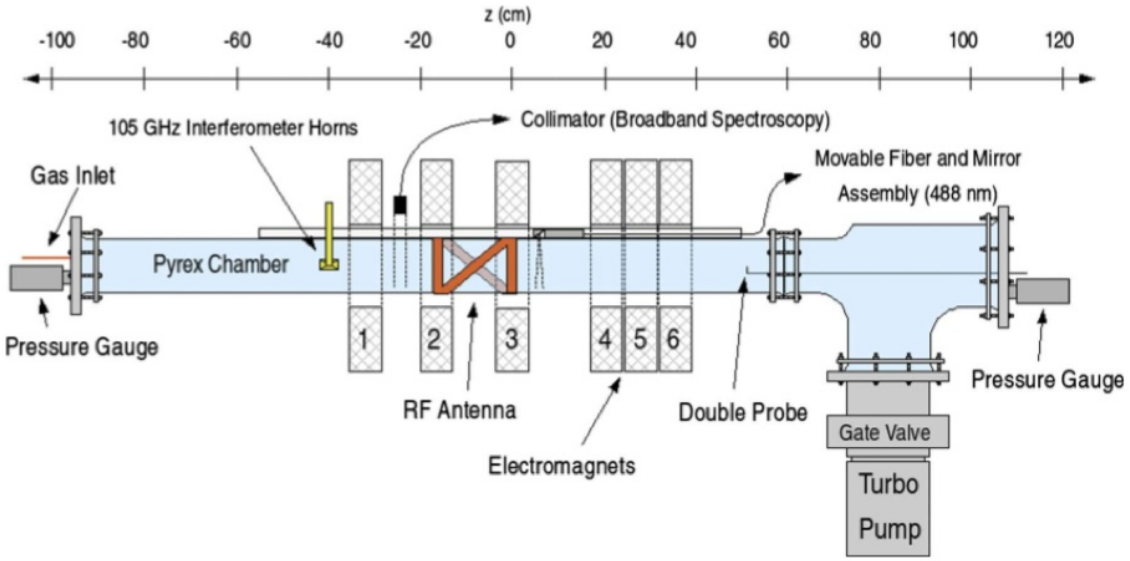

Figure 1. Madison Helicon Experiment (MadHeX).

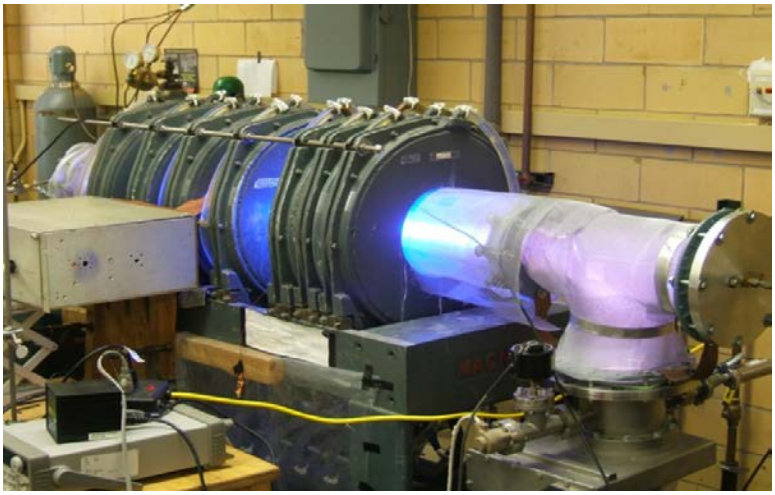

Figure 2. Operation of MadHEx at 3 kW input power.

A photo of a larger (45 cm) diameter expansion chamber to allow the plasma and magnetic field lines to diverge and reduce neutral reflux is shown in Figure 3.

It should be noted that our system is in a flowing configuration. The argon gas is fed in the upstream side of the chamber and is pulled through the antenna region by the downstream turbopump. This configuration can help mitigate any neutral starvation.

RF power up to 10 kW is used to produce steady-state helicon plasmas in a static magnetic field that can be configured in a flat or mirror profile, with a current magnetic field strength of 1.04 kG in the antenna source region with a 1.5 kG mirror peak that can be readily doubled to 3 kG. Millimeter wave (105 GHz)

Figure 3. MadHeX Expansion Chamber, not installed in system.

interferometry that we have developed to high level of expertise[19–21] is used to determine the line-averaged electron density (n_e). The comparison of excited state populations of Ar I and Ar II with two different collisional-radiative (CR) models provides a non-invasive technique to measure the line-averaged electron temperature (T_e) and neutral density (n_n). The electron temperature is determined using the ADAS CR model,[22,23] while n_n is determined using a CR model developed by Vlcek.[24] A movable narrow beam (3 degree) horn-reflector system allowing density profile measurements from the source region through the magnetic nozzle to the exhaust region will be utilized to provide continuous, non-invasive density profiles. The axial ion velocity and temperature is measured through diode-based laser-induced fluorescence (LIF).

B. Diagnostics

1. Microwave Interferometry

A 105 GHz Mach-Zehnder millimeter-wave interferometer is used to determine the electron density (n_e), line-averaged over the 10 cm chamber diameter. For O-mode propagation, the phase shift varies linearly with the electron density (in cm^{-3}) as follows:

$$n_e = 2.07 f \Delta\phi / d \tag{1}$$

where f is the interferometer frequency (Hz), d is the chamber diameter (cm), and $\Delta\phi$ is the phase shift (degrees).[19] Using radial density profiles measured by a Langmuir probe at lower (< 1 kW) powers, the peak electron density can be determined. Interferometer measurements in the magnetized source region are only possible where there are sufficient gaps between the electromagnets to position the microwave horns. The nozzle configuration allows measurements between the magnets at z = -25 cm and 11 cm, while the flat field configuration allows for downstream measurements at a third position, z = 22 cm. Unrestricted measurements are possible beyond the magnets, from the upstream endplate at z = -91 to -40 cm, and from z = 42 cm to the downstream endplate at z = 105 cm. The helical antenna and rf feeds make measurement between magnets 2 and 3 (z = -18 to 0 cm) impractical.

2. Optical Spectroscopy and Collisional Radiative Modelling

T_e and neutral density (n_n) are measured using broadband ion (Ar II) and neutral (Ar I) optical spectra, respectively. These parameters are determined using two different collisional-radiative (CR) models that calculate excited population densities that can be compared to those measured optically.

To determine the electron temperature and neutral density, the radiance of each line of interest is measured using an absolutely calibrated Ocean Optics ST2000 spectrometer, which is required to calculate the

excited state population number densities required by the CR model codes. The optical emission is collected by a collimator and is coupled into a trifurcated fiber which delivers the light to three separate gratings and CCD arrays which are sensitive to three different bands (200 - 500 nm, 400 700 nm, and 600 - 870 nm). Once determined spectroscopically, the excited state population densities can then be compared with densities predicted by the collisional-radiative codes to determine T_e and n_n.

T_e is determined with data computed using the Atomic Data and Analysis Structure (ADAS) CR model for argon ions. The code and technique we use to determine T_e with the ADAS model is based on and is very similar to that originally developed by Sciamma.[23] One can determine T_e by finding the coefficients that result in the computationally-determined excited populations that match with the spectroscopically measured excited populations for the measured n_e. Since the code requires input of both n_e and T_e it is necessary to know one of the quantities to determine the other. We have used the code to determine T_e with the experimentally determined ne, though in principle the reverse can be performed.

The Ar I CR model used to determine n_n was originally formulated by Vlcek.[24] The code we use incorporating the Vlcek model is based on and operationally identical to code written by Keesee[25] and later adapted by Sciamma.[23] Unlike the method used to determine T_e, the Ar I CR code solves these equations for the various level populations rather than using precalculated tables. The code requires inputs of both n_e and T_e, the latter of which can be determined by the ADAS CR code, and assumes quasineutrality and singly-ionized ions, as does the ADAS model. The neutral density is determined by finding the neutral density that, when entered into the code, results in level parent populations that correspond most closely with those measured spectroscopically.

The collisional-radiative spectroscopic diagnostics assume that no significant populations of doubly-ionized or higher ionization states are present ($Z > 1$). In order to verify this, optical spectra were measured to compare the emission levels for Ar II lines (found between 350 and 525 nm) and those for Ar III (found primarily in the UV band between 300 and 350 nm). The spectra were measured for the highest power level used (3 kW) and at the axial location where the ionization levels were the highest ($z = 11$ cm). Accounting for UV transmission through the Pyrex and the calibrated instrument sensitivity in these two bands, the Ar II lines were found to be approximately 50 times stronger than the Ar III lines, indicating that the doubly-ionized population is indeed negligible under these conditions.[17]

3. Laser Induced Fluorescence

The MadHeX experiment uses laser induced fluorescence (LIF) to measure the ion energy distribution in our plasma. The key component of this diagnostic is our tunable diode laser system. Our group recently acquired a master oscillator power amplifier (MOPA) system that has a maximum laser output power of 500 mW at 668.6 nm. By measuring the shift in wavelength of a particular argon ion line excited by the tunable laser, the ion energy distribution and therefore the ion beam velocity and temperature.

The MOPA LIF system is shown below in Figure 4. A room temperature iodine gas cell is used as a reference during LIF operation. The iodine cell emission is compared to known emission lines and the precise wavelength of the LIF laser can be determined as its wavelength is swept. A Burleigh wavemeter is used to tune the laser initially and is removed from the beamline for operation. An axially-movable mirror and optics system placed on the top of the Pyrex chamber is used to collect LIF-laser-stimulated argon ion (432.6 nm) emission that is analyzed using a PMT attached to a 0.5m ACTON monochromator. The LIF laser is chopped using a mechanical chopper and lock in amplifiers are used to analyze both the collected iodine (reference) and argon ion emission.

III. Results

A. Neutral Depletion

Figure 5(a) shows the variation of electron density (microwave interferometry), electron temperature (ADAS collisional radiative modeling) and neutral density (Vlcek collisional radiative modeling). Two distinct regions exist in the system:

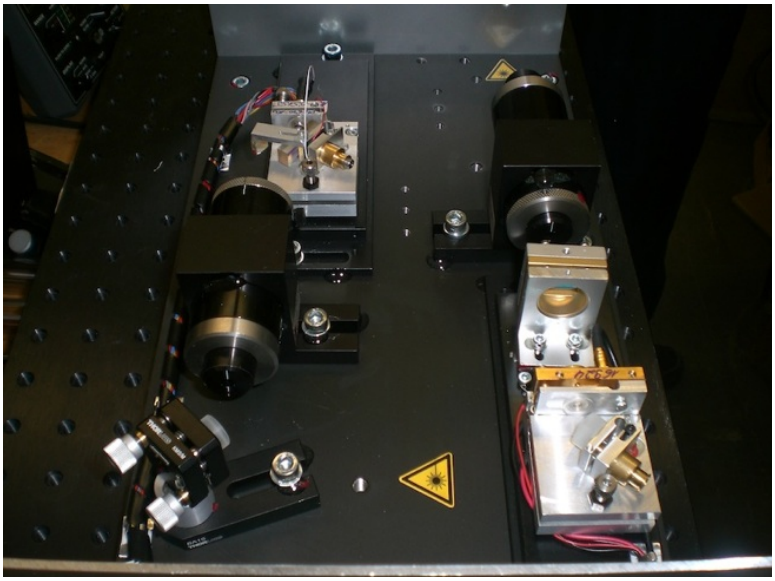

Figure 4. LIF MOPA System.

1. Upstream of the RF antenna (z = -50 cm to z = -18 cm)

In the upstream region, increasing input power serves to ionize additional argon. There is increasing electron density and decreasing neutral density, while electron temperature remains low near 2 eV with a slight increase with input power. Electron density reaches 1.6 x 10^{12} cm^{-3} line averaged at 3 kW and neutral density decreases by an order of magnitude.

2. Downstream of the RF antenna (z = -18 cm to z = 50 cm)

In the downstream region, increasing input power serves to heat electrons. Neutral density is low both at 500 W and 3 kW (compared to the upstream region). Electron density remains nearly the same for both 500 W and 3 kW, but electron temperature roughly doubles. The plasma in the downstream region is almost fully ionized (92% line averaged).

B. Total Pressure Variation

Figure 5(b) shows the variation of total pressure at several axial locations at 0 W, 500 W and 3 kW input power. The upstream and downstream points are measured by the pressure gauges located at each position. The upstream region is in pressure balance, whereas there is a pressure gradient in the antenna region and through the downstream region. This results in a plasma flow, which can be estimated using flux conservation using the known electron (ion) density at each location and assuming full argon ionization in steady state. For 3 kW input power, the upstream plasma flow velocity is v_i = 250 m/s and the downstream flow is v_i = 550 m/s at 76 sccm steady state flow rate. The highly ionized plasma with T_i = 0.1 eV has an ion neutral mean free path of several meters so that the plasma is collisionless and the electrostatic shock and double layer ion acceleration region can form. The pressure variation at this flow rate is substantial and yields an increased plasma flow due to the reduced neutral concentrations downstream from the antenna.

This process is self-consistent. The plasma density that drives the pressure gradient is a function of the pressure gradient itself, due to flux conservation. The decreased neutral density in the downstream region allows for enhanced plasma flow due to reduced neutral drag on the ions.

C. Pulsed Operation

Recent pulsed operation (5 ms period) has revealed interesting transient dynamics during the pulse. A high-density peak, up to 4 x 10^{13} cm^{-3} line averaged (~8 x 10^{13} cm^{-3} peak) occurs and then the system relaxes to a neutrally depleted steady state. Steady state is reached in as little as 5 ms.

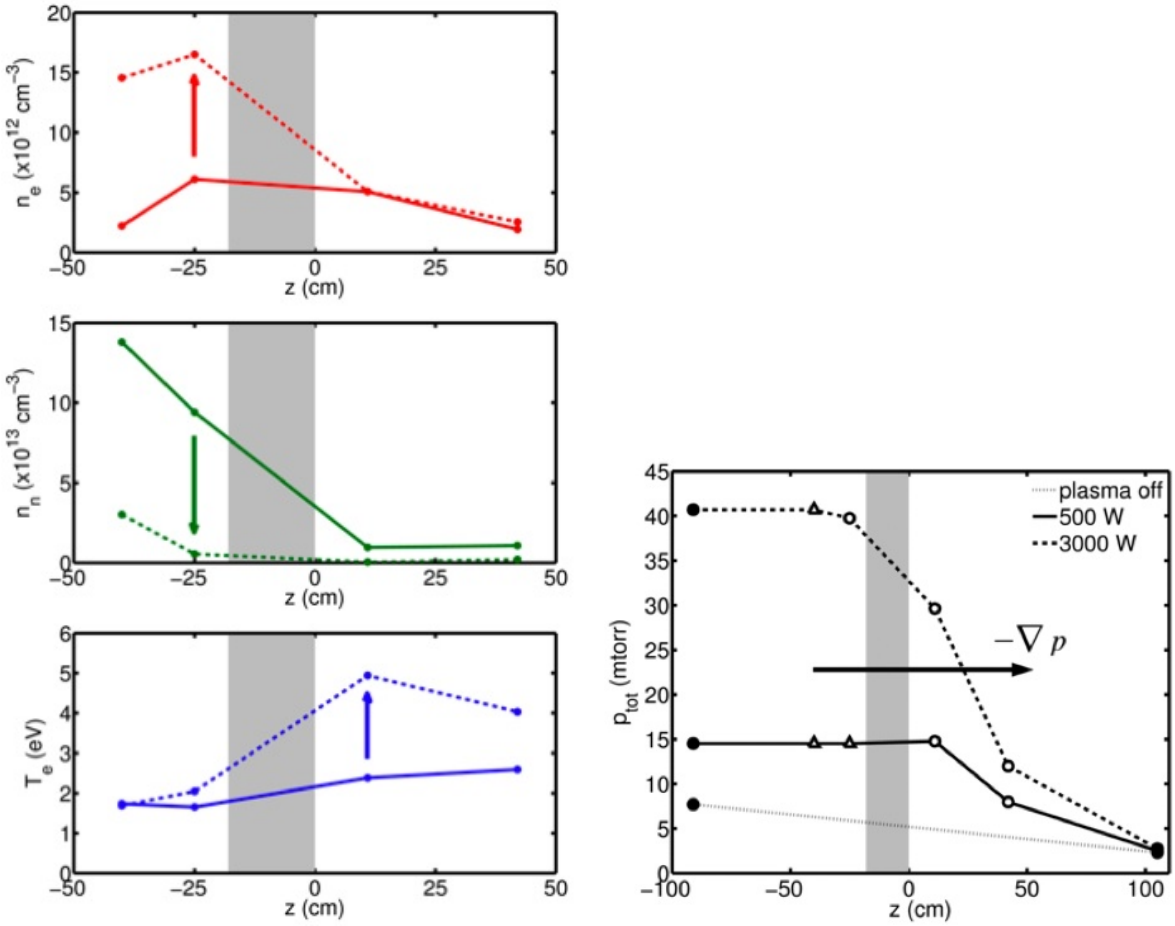

Figure 5. (a) Variation of n_e, n_n, and T_e along the experimental axis for input powers of 500 W (solid) and 3000 W (dashed). (Flow rate of 76 sccm with 1 kG nozzle-configuration field.) The shaded area indicates antenna extent, (b) Total pressure (p_{tot}) for 76 sccm over the entire axial extent of the chamber (z=91 to 105 cm) for plasma off (dotted) as well as 500 W (solid) and 3000 W (dashed) rf power conditions. p_{tot} is assumed to be dominantly p_n (solid circles), p_e (open circles) and $p_n + p_e$ (triangles) at various points. The shaded area indicates the antenna extent.

The initial density peak is due to the initial ionization of a population of neutrals very near the antenna. The ionization leads to a pressure gradient which drives the ions from the source region. Figure 6 illustrates the electron density during pulsed operation at 6 kW, B = 760 G and a 76 sccm flow rate. Reduced plasma density upstream and well downstream of the nozzle is observed as well. The reduced downstream density in this case is due to plasma acceleration due to neutral depletion and corresponds to a flow velocity of 1300 m/s flowing into the nozzle region where an electrostatic shock double layer and ion acceleration are expected at lower flow rates.

D. Laser Induced Fluorescence

Figure 6 illustrates our initial MOPA LIF higher power 1 kW measurement of the ion bulk drift just beyond the nozzle at a 20 sccm flow rate corresponding to pressures of 0.8 mtorr in the downstream region. It illustrates a bulk argon ion drift of 2 km/s. Further LIF measurements at lower sccm flow rates and higher power levels with larger beam formed Doppler shifts are and will be made in the future to demonstrate the helicon plasma source for thruster applications.

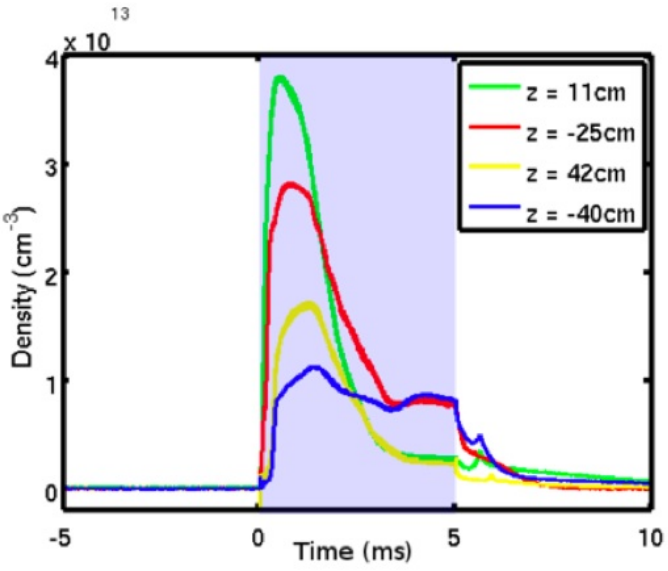

Figure 6. Line averaged electron density (n_e) during pulsed operation as a function of time and axial distance.

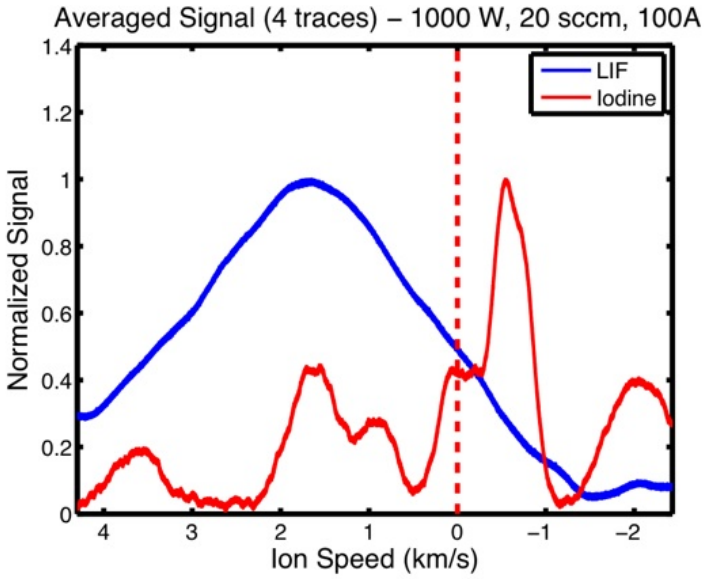

Figure 7. Laser Induced Fluorescence Signal. Power is 1 kW, flow rate is 20 sccm argon at z=42 cm.

E. Low Pressure Operation

Recent interest in low pressure initiation of helicon or inductive plasma discharges has prompted us to investigate the ability of MadHeX to start up at low flow rates and pressures. An interesting phenomenon was observed. When the gas flow rate was below 14 sccm (corresponding to an upstream pressure of 2.5 mtorr and a downstream pressure of 0.6 mtorr) a discharge cannot be started if the static magnetic field is above a threshold value. This is interpreted using multipactor arguments. As the flow rate is decreased, the probability of a collisional ionization event occurring in the experiment decreases (the mean free path for ionization becomes longer than the system length). The breakdown mechanism shifts to multipactor, a resonant process occurring near the chamber walls. The multipactor process is likely occurring when the gas flow rate is higher than the threshold rate (14 sccm) but becomes the dominant mechanism when the mean free path for ionization becomes larger than the system dimensions. The magnetic field breaks the

multipactor resonance condition at high field values and the discharge will not begin.[26]

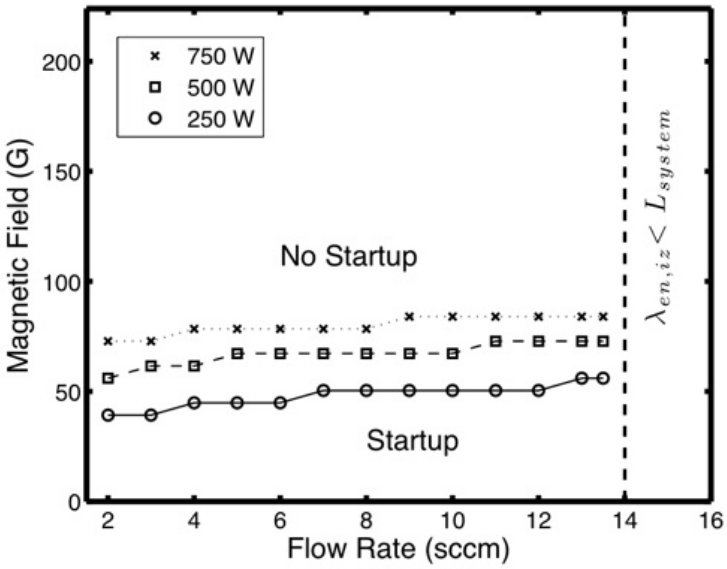

Figure 8. Low Pressure Discharge Initiation Threshold.

Shown in Figure 8 is the threshold magnetic field value for discharge initiation as a function of rf input power and gas flow rate. Above the threshold field value, discharges will not reliably start, or will not start at all. Long exposure photographs of the system in darkness with no argon flow (system at base pressure of 10^{-6} Torr) revealed a multipactor-induced glow that can be started and stopped by lowering and raising the magnetic field, providing evidence of multipactors role in discharge initiation.

IV. Conclusion

We have demonstrated non-invasive millimeter wave interferometer, optical spectroscopy and LIF methods for illustrating the properties of helicon plasma sources at coupled power levels up to 10 kW. The RF power is readily coupled and produces highly ionized plasma with observed ionization of >92% (line averaged) downstream from the antenna. Neutral depletion processes increase the fully ionized plasma flow as it enters the nozzle and double layer regions. By examining lower flow rate and higher power levels, we plan to produce fast electron components to the helicon source distribution that will further enhance ion acceleration and thruster performance.

Acknowledgments

This research is supported in part by the Air Force Office of Scientific Research, grant number AFOSR Grant FA9550-09-1-0357, as well as the University of Wisconsin - Madison.

References

1. F. F. Chen, *Plasma Physics and Controlled Fusion*. Plenum Press, NY, 1984.

2. J. Scharer, A. Degeling, G. Borg, and R. Boswell, "Measurements of helicon wave propagation and ArII emission," *Physics of Plasmas*, vol. 9, no. 9, pp. 3734–3742, 2002.

3. S. M. Tysk, C. M. Denning, J. E. Scharer, and K. Akhtar, "Optical, wave measurements, and modeling of helicon plasmas for a wide range of magnetic fields," *Physics of Plasmas*, vol. 11, no. 3, pp. 878–887, 2004.

4. V. F. Virko, K. P. Shamrai, Y. V. Virko, and G. S. Kirichenko, "Wave phenomena, hot electrons, and enhanced plasma production in a helicon discharge in a converging magnetic field," *Physics of Plasmas*, vol. 11, no. 8, pp. 3888–3897, 2004.

5. F. Chen and R. Boswell, "Helicons-the past decade," *Plasma Science, IEEE Transactions on*, vol. 25, no. 6, pp. 1245–1257, Dec 1997.

6. Y. Mouzouris, J. E. Scharer, and M. Bettenhausen, "Wave Absorption Mechanisms and Transport for a Helicon Source Operation," *APS Meeting Abstracts*, pp. 4–+, Nov. 1996.

7. R. L. Kinder and M. J. Kushner, "Noncollisional heating and electron energy distributions in magnetically enhanced inductively coupled and helicon plasma sources," *Journal of Applied Physics*, vol. 90, no. 8, pp. 3699–3712, 2001.

8. G. G. Borg, J. Bright, and I. V. Kamenski, "Collisionless energy coupling to high-velocity electrons in the near field of an antenna: neutral gas ionization by helicon waves," *Plasma Physics and Controlled Fusion*, vol. 40, pp. 987–1000, Jun. 1998.

9. A. W. Degeling and R. W. Boswell, "Modeling ionization by helicon waves," *Physics of Plasmas*, vol. 4, no. 7, pp. 2748–2755, 1997.

10. R. T. S. Chen and N. Hershkowitz, "Multiple electron beams generated by a helicon plasma discharge," *Phys. Rev. Lett.*, vol. 80, no. 21, pp. 4677–4680, May 1998.

11. A. W. Degeling, T. E. Sheridan, and R. W. Boswell, "Model for relaxation oscillations in a helicon discharge," *Physics of Plasmas*, vol. 6, no. 5, pp. 1641–1648, 1999.

12. A. I. Akhiezer, V. S. Mikhailenko, and K. N. Stepanov, "Ion-sound parametric turbulence and anomalous electron heating with application to helicon plasma sources," *Physics Letters A*, vol. 245, no. 1-2, pp. 117 – 122, 1998.

13. V. S. Mikhailenko, K. N. Stepanov, and E. E. Scime, "Strong ion-sound parametric turbulence and anomalous anisotropic plasma heating in helicon plasma sources," *Physics of Plasmas*, vol. 10, no. 6, pp. 2247–2253, 2003.

14. M. Kramer, Y. M. Aliev, A. B. Altukhov, A. D. Gurchenko, E. Z. Gusakov, and K. Niemi, "Anomalous helicon wave absorption and parametric excitation of electrostatic fluctuations in a helicon-produced plasma," *Plasma Physics and Controlled Fusion*, vol. 49, no. 5A, pp. A167–A175, 2007.

15. M. M. Balkey, R. Boivin, J. L. Kline, and E. E. Scime, "Ion heating and density production in helicon sources near the lower hybrid frequency," *Plasma Sources Science Technology*, vol. 10, pp. 284–294, May 2001.

16. E. Ahedo and M. M. Sanchez, "The role of current-free double-layers in plasma propulsion," *44th AIAA/ASME/SAE/ASEE Joint Propulsion Conference & Exhibit, 21 - 23 July 2008, Hartford, CT*.

17. C. M. Denning, M. Wiebold, and J. E. Scharer, "Observations of neutral depletion and plasma acceleration in a flowing high-power argon helicon plasma," *Physics of Plasmas*, vol. 15, no. 7, p. 072115, 2008.

18. X. M. Guo, J. Scharer, Y. Mouzouris, and L. Louis, "Helicon experiments and simulations in nonuniform magnetic field configurations," *Physics of Plasmas*, vol. 6, no. 8, pp. 3400–3407, 1999.

19. S. Luo, J. E. Scharer, M. Thiyagarajan, and C. M. Denning, "Experimental study of laser-initiated radiofrequency-sustained high-pressure plasmas," *Plasma Science, IEEE Transactions on*, vol. 34, no. 6, pp. 2637–2651, Dec. 2006.

20. K. Akhtar, J. E. Scharer, S. M. Tysk, and E. Kho, "Plasma interferometry at high pressures," *Review of Scientific Instruments*, vol. 74, no. 2, pp. 996–1001, 2003.

21. S. Luo, C. M. Denning, and J. E. Scharer, "Laser-rf creation and diagnostics of seeded atmospheric pressure air and nitrogen plasmas," *Journal of Applied Physics*, vol. 104, no. 1, p. 013301, 2008.

22. "Adas website, http://www.adas.ac.uk."

23. E. Sciamma, "Plasma spectroscopic diagnostic tool using collisional-radiative models and its application to different plasma discharges for electron temperature and neutral density determination," Ph.D. dissertation, The University of Texas at Austin, 2007.

24. J. Vlcek, "A collisional-radiative model applicable to argon discharges over a wide range of conditions. i. formulation and basic data," *Journal of Physics D: Applied Physics*, vol. 22, no. 5, pp. 623–631, 1989.

25. A. M. Keesee and E. E. Scime, "Neutral argon density profile determination by comparison of spectroscopic measurements and a collisional-radiative model (invited)," *Review of Scientific Instruments*, vol. 77, no. 10, p. 10F304, 2006.

26. M. Wiebold, H. Ren, C. M. Denning, and J. E. Scharer, "Low pressure helicon discharge initiation via magnetic field ramping," *IEEE Trans. on Plasma Sciences*, Accepted for Publication.